Wave equation migration velocity analysis with time-shift imaging condition

Claudio Guerra and Biondo Biondi

ABSTRACT

We introduce a new objective function for wave-equation migration velocity analysis. This objective function borrows the main idea of the differential semblance optimization, but instead of applying this operator in the subsurface-offset or aperture angle gathers, we apply it in the time-shift gathers computed by time-shift imaging condition. Using a simple model of two Gaussian velocity anomalies, we show image and slowness perturbations by applying the forward and adjoint tomographic operators and image perturbation and the gradient of the objective function after differential semblance operator on time-shift gathers. The results are promising.

INTRODUCTION

more still to come ....

Wave-equation migration velocity analysis (WEMVA)(Sava, 2004; Sava and Biondi, 2004) promises to overcome the limitations of migration velocity analysis due to the high-frequency approximation, which consider rays as carriers of information. WEMVA uses band-limited perturbed source and receiver wavefields and scattered source and receiver wavefields to compute the gradient of the objective function that back-propagates the slowness perturbation through the model space. The scattered wavefields are computed by applying the scattering operator (Huang et al., 1999) on the background wavefields, while perturbed wavefields are computed by convolving the background receiver and source wavefields, respectively, with a perturbed image. The objective function is represented by some norm of the perturbed image and reflects the correctness of the slowness model.

In the differential semblance velocity analysis (DVSA) (Shen and Symes, 2008), the perturbed image is obtained via differential semblance optimization (DSO). DSO can be applied on both subsurface-offset gathers or aperture-angle gathers. Since there is no residual moveout interpretation, the objective function is fully automated and the velocity inversion can be carried out by Quasi-Newton methods, like L-BFGS (Shen and Symes, 2008).

more still to come .... Sava and Fomel (2006) introduce the time-shift imaging condition, in which source and receiver wavefields are phase shifted prior to correlation.

The kinematic properties of these image gathers have been explored to perform velocity update, after transformation to reflection-angle gathers (Liu and Wang, 2007).

In this paper we investigate the use of time-shift image gathers in DVSA. We start by briefly describing the forward and adjoint WEMVA operators; then we explain the time-shift imaging condition; proceed to develop the new objective function resultant of applying DSO-like operator on those image gathers; and finalize by showing some numerical examples.

FORWARD AND ADJOINT WEMVA OPERATORS

TIME-SHIFT IMAGING CONDITION

Based on the theory of reflector mapping (Claerbout, 1971), the image is formed at points where source and receiver wavefields coincide both in time of wavefield propagation and spatially. In the context of migration by downward-continuation, this translates into point-wise multiplying the receiver wavefield, R, with the complex conjugate of the source wavefield, S^*, at every image location, $\mathbf{x}$, and summing over all frequencies, ω, which represents to extract the image, I,at zero time. For a single shot we have

$$I(\mathbf{x}) = \sum_{\omega} S^*(\mathbf{x},\omega) R(\mathbf{x},\omega). \tag{1}$$

This imaging condition, however, does not yield an image suited for estimating velocity errors. To overcome the limitation of the above imaging condition, different generalizations have been proposed (Rickett and Sava, 2002; Biondi and Symes, 2004; Sava and Fomel, 2005). They consist of spatially shifting the wavefields with respect to each other prior to the point-wise multiplication. The spatial shifts are interpreted as subsurface offsets, $\mathbf{h}$, which can be computed in any direction. For the case of complete acquisition aperture and correct velocity, negligible amplitudes are computed for subsurface offsets different from zero. Departures from the zero offset are indicative of illumination problems or velocity errors. In general, the image is computed by

$$I(\mathbf{x},\mathbf{h}) = \sum_{\omega} S^*(\mathbf{x}-\mathbf{h},\omega) R(\mathbf{x}+\mathbf{h},\omega). \tag{2}$$

Sava and Fomel (2006) introduced the space- and time-shift imaging condition, from which the time-shift imaging condition is a special case. It is computed by applying a phase-shift to the wavefields prior to summation over frequencies

$$I(\mathbf{x},\tau) = \sum_{\omega} S^*(\mathbf{x},\omega) R(\mathbf{x},\omega) \mathbf{e}^{\mathbf{i2}\omega\tau}. \tag{3}$$

Time-shift image gathers present linear events with slope equal to the local velocity at the reflector. If migration is performed with a faster velocity, energy concentrates at

negative time-shifts and shallower than the correct depth, indicating that source and receiver rays cross above the imaging point (where $\tau = 0$). If migration is performed with a slower velocity, energy concentrates at positive time-shifts and deeper than the correct depth, indicating that rays cross below the imaging point. For the case of correct velocity, energy concentrates at $\tau = 0$.

USING TIME-SHIFT IMAGING CONDITION FOR VELOCITY UPDATE

Sava and Fomel (2006) show that time-shift image gathers can be transformed into angle-domain common image gathers by slant-stacking. In 2D, the transformation can be carried out by a Radon transform

$$I(z, x, \gamma) = \int I(z, x, \tau) d\tau|_{\zeta(\gamma,\alpha,\tau)}, \tag{4}$$

where γ is apparent the reflection angle, α is the apparent geological dip, and

$$\zeta(\gamma, \alpha, \tau) = z + v\tau \sec\alpha \sec\gamma \tag{5}$$

is the stacking path.

This transformation yields images suited for velocity update. Using angle gathers, in wave-equation migration velocity analysis (Sava and Biondi, 2003), a residual moveout parameter is picked and used to compute the image perturbation. Shen and Symes (2008) use angle gathers, computed from subsurface offset gathers, to obtain the perturbed image by applying the differential semblance operator (DSO). They show that the results of velocity inversion using DSO in the angle domain ($\mathbf{D}_\gamma$) to compute the image perturbation are of lower quality than that obtained using DSO in the offset domain ($\mathbf{D_h}$). They claim that the different performances are due to the fact that the Hessian is better conditioned in the case of the offset domain DSO.

To apply a DSO-like strategy when using time-shift image gathers, transformation to the angle domain requires information about the geological dip. If this information is not available or not reliable, the slant-stack transformation should include the apparent geological dip dimension, turning the computation of the perturbed image more expensive. So, it is desirable to derive an offset-domain DSO-like operator to be used in the time-shift gathers.

The equivalence between the time-shift DSO ($\mathbf{D}_\tau$) with $\mathbf{D}_\gamma$, if exists, can be expressed by

$$\mathbf{D}_\tau I(\mathbf{x}, \tau) = \mathbf{R}_\gamma^{-\mathbf{1}} \mathbf{D}_\gamma \mathbf{R}_\gamma I(\mathbf{x}, \tau), \tag{6}$$

where $\mathbf{R}_\gamma$ is the time-shift to angle transformation (equation 4). The perturbed image, after application of forward and adjoint operators on the background image, is

$$\mathbf{D}_\tau^* \mathbf{D}_\tau I(\mathbf{x}, \tau) = \mathbf{R}_\gamma^* \mathbf{D}_\gamma^* \mathbf{D}_\gamma \mathbf{R}_\gamma I(\mathbf{x}, \tau). \tag{7}$$

Recalling that $\mathbf{D}_\gamma = \frac{\partial}{\partial \mathbf{q}}$, where $q = \sec\gamma$, and that equation 5 can be written as

$$\begin{aligned}
\mathbf{R}_\gamma I(z,x,\tau) &= \int I(z+qv\tau\sec\alpha, x, \tau)\, d\tau \\
&= \int\int I(\varsigma, x, \tau)\delta(\varsigma - z - qv\tau\sec\alpha)\, d\varsigma\, d\tau \\
&= \int\int\int I(\varsigma, x, \tau) e^{ik_\varsigma(\varsigma - z - qv\tau\sec\alpha)} d\varsigma\, d\tau\, dk_\varsigma, \qquad (8)
\end{aligned}$$

we have

$$\begin{aligned}
\mathbf{D}_\tau^*\mathbf{D}_\tau I(z,x,\tau) &= \mathbf{R}_\gamma^* \int\int\int -\frac{\partial^{\mathbf{2}}}{\partial \mathbf{q^2}} I(\varsigma, x, \tau) e^{ik_\varsigma(\varsigma - z - qv\tau\sec\alpha)} d\varsigma\, d\tau\, dk_\varsigma \\
&= \mathbf{R}_\gamma^* \int\int\int (v\tau\sec\alpha k_\varsigma)^2 I(\varsigma, x, \tau) e^{ik_\varsigma(\varsigma - z - qv\tau\sec\alpha)} d\varsigma\, d\tau\, dk_\varsigma. \qquad (9)
\end{aligned}$$

By moving the adjoint of the Radon transform inside the integral, and writing $\xi = v\sec\alpha$, we obtain

$$\begin{aligned}
\mathbf{D}_\tau^*\mathbf{D}_\tau I(z,x,\tau) &= \int\int \left[\int\int\int (\xi\tau k_\varsigma)^2 I(\varsigma', x, \tau') e^{ik'_\varsigma(\varsigma' - z - \xi q\tau')} d\varsigma'\, d\tau'\, dk'_\varsigma\right] e^{-ik_\varsigma(\varsigma - z - \xi q\tau)} dq\, dk_\varsigma \\
&= \int\int\int\int (\xi\tau k_\varsigma)^2 I(\varsigma', x, \tau') e^{ik_\varsigma(\varsigma' - \varsigma)} e^{ik_\varsigma q\xi(\tau' - \tau)} dq\, d\tau'\, d\varsigma'\, dk_\varsigma \\
&= \int\int\int (\xi\tau k_\varsigma)^2 I(\varsigma', x, \tau') e^{ik_\varsigma(\varsigma' - \varsigma)} \left[\int e^{ik_\varsigma \xi q(\tau' - \tau)} dq\right] d\tau'\, d\varsigma'\, dk_\varsigma. \qquad (10)
\end{aligned}$$

In the bracketed term, one can recognize the Fourier transform of $\frac{\delta(\tau' - \tau)}{[k_\varsigma \xi]}$. So, equation 10 reads

$$\mathbf{D}_\tau^*\mathbf{D}_\tau I(z,x,\tau) = \int\int \tau^2 \left|\xi k_\varsigma\right| I(\varsigma', x, \tau) e^{ik_\varsigma(\varsigma' - \varsigma)} d\varsigma'\, dk_\varsigma. \qquad (11)$$

Finally, using the relation

$$\int |k|\, e^{ikx} dk = \frac{-2}{x^2}$$

we get

$$\mathbf{D}_\tau^*\mathbf{D}_\tau I(z,x,\tau) = -2\tau^2 v \left|\sec\alpha\right| \int \frac{I(\varsigma', x, \tau)}{(\varsigma' - \varsigma)^2} d\varsigma'. \qquad (12)$$

Equation 12 shows that the operator $\mathbf{D}_\tau$ is similar to $\mathbf{D_h}$, except for the scaling by the absolute value of the secant of the apparent geological dip and local velocity. The perturbed image can be computed by applying the $|\tau|$ operator. However, the spread of energy along the line with slope equal to the local velocity poses a problem to $\mathbf{D}_\tau$. Even if it is used the correct velocity, the perturbed image will present strong amplitudes away from the zero time.

To circumvent this problem, we use a simple thresholding strategy prior to $\mathbf{D}_\tau$, such that the spread energy is zeroed out. more still to come ...

NUMERICAL EXAMPLES

To test the potential of using time-shift image gathers in wave-equation migration velocity analysis, we use a simple model of two Gaussian anomalies located at (-800,800) and (800,800) embedded in a background velocity of 2000m/s. A reflector is positioned at a depth of 1500m. The Gaussian anomaly at negative x position has 10% slower velocity than the background and the Gaussian anomaly located at positive x position has 10% faster velocity than the background. We used one-way Born modeling to generate 81 shots with 100m spacing, maximum offset of 6000m, and receiver interval equals to 10m. Figure 1 shows the image computed with a background velocity of 2000m/s and time-shift imaging condition.

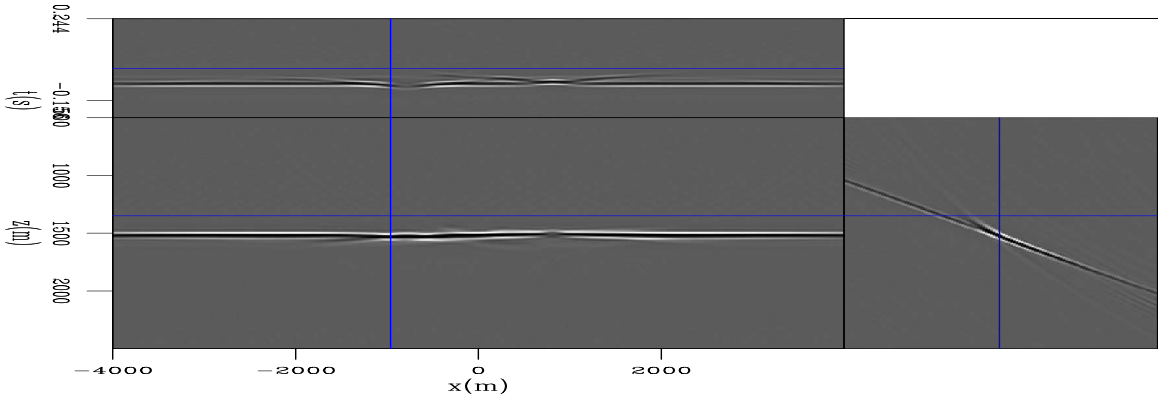

Figure 1: Background image computed time-shift imaging condition.[**CR**]

Using a background velocity of 2000m/s, we computed the perturbed image by applying the forward tomographic operator in the shot-profile domain. In this case, the slowness perturbation (Figure 2) is known beforehand. Figure 3 shows the perturbed image.

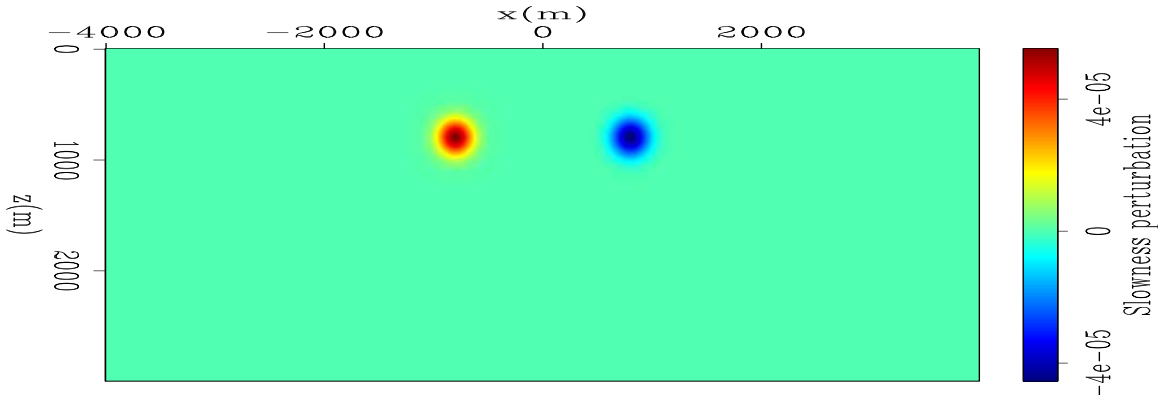

Figure 2: Slowness perturbation used to compute the image perturbations of Figures 3 and 5.[**ER**]

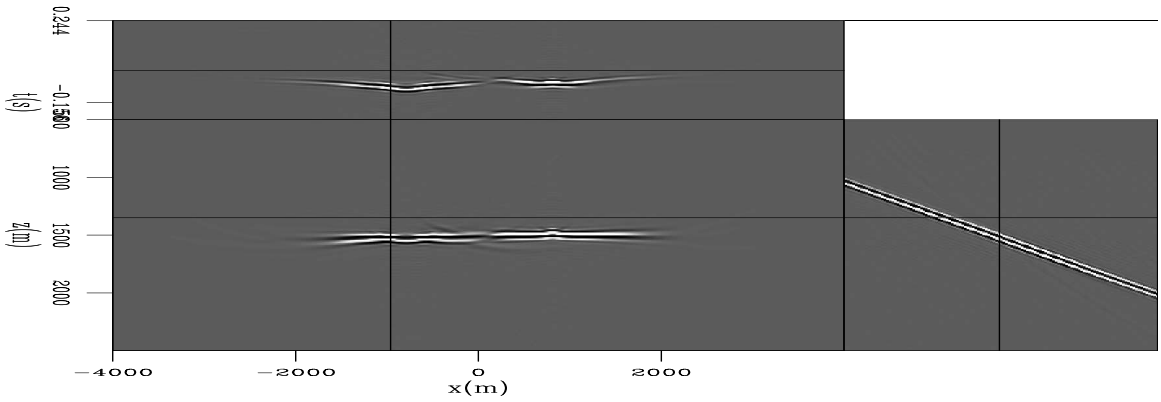

Figure 3: Image perturbation computed with the slowness perturbation of Figure 2 and time-shift imaging condition.[**CR**]

The perturbed image of Figure 3 was used to compute the slowness perturbation by applying the adjoint of the tomographic operator. The predicted slowness perturbation is shown in Figure 4. Strong artifacts occur due to the poor shot sampling. However, it is noticeable that the correct signal of the slowness perturbation is recovered.

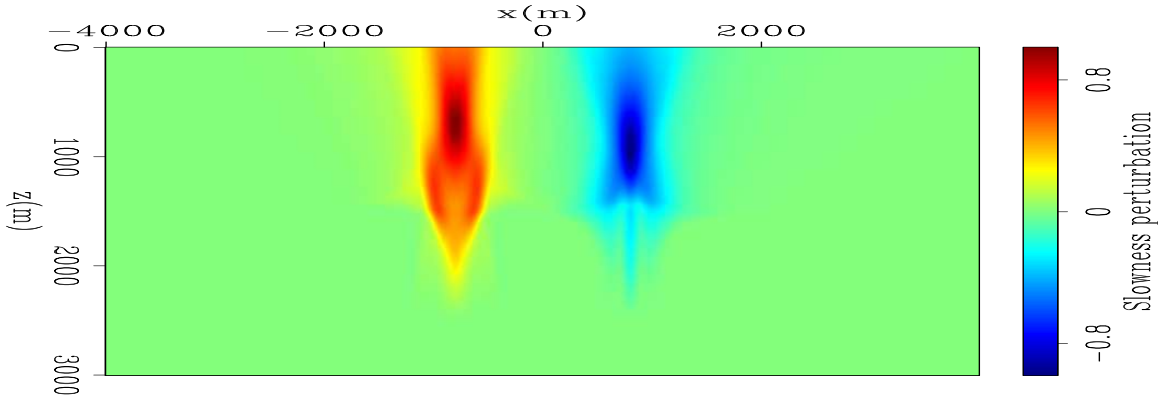

Figure 4: Predicted slowness perturbation computed with the image perturbation of Figure 3 and time-shift imaging condition.[**CR**]

For comparison, we show the perturbed image (Figure 5) and the the slowness perturbation (Figure 6) computed for the case of space-shift imaging condition. The clip of the amplitudes of the space-shift slowness perturbation is different from the time-shift slowness perturbation to highlight its general structure. Overall, both slowness perturbations show a similar pattern. However, the effect of poor shot sampling is more pronounced in the time-shift slowness perturbation than in the space-shift slowness perturbation.

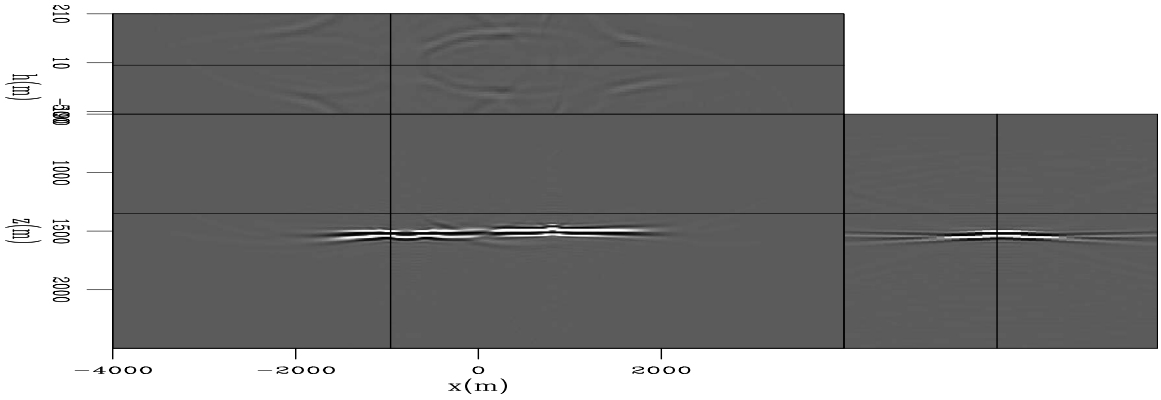

Figure 5: Image perturbation computed with the slowness perturbation of Figure 2 and using space-shift imaging condition.[**CR**]

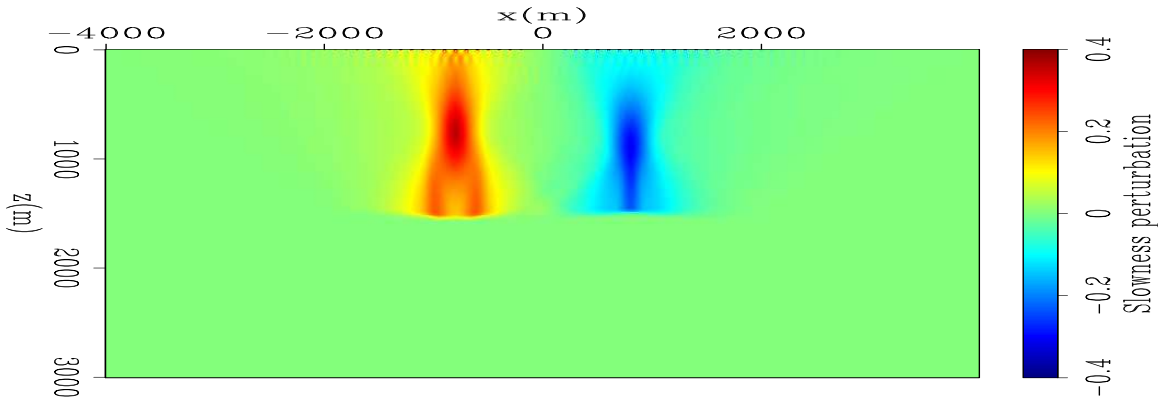

Figure 6: Predicted slowness perturbation computed with the space-shift image perturbation of Figure 5 and space-shift imaging condition.[**CR**]

CONCLUSIONS

REFERENCES

Biondi, B. and W. W. Symes, 2004, Angle-domain common-image gathers for migration velocity analysis by wavefield-continuation imaging: Geophysics, **69**, 1283–1298.

Claerbout, J. F., 1971, Toward a unified theory of reflector mapping: Geophysics, **36**, 467–481.

Huang, L.-J., M. C. Fehler, and R.-S. Wu, 1999, Extended local born fourier migration method: Geophysics, **64**, 1524–1534.

Liu, S. and H. Wang, 2007, Time-shift angle-domain common-image gathers for migration velocity analysis: SEG Technical Program Expanded Abstracts, **26**, 2797–2801.

Rickett, J. E. and P. C. Sava, 2002, Offset and angle-domain common image-point gathers for shot-profile migration: Geophysics, **67**, 883–889.

Sava, P., 2004, Migration and velocity analysis by wavefield extrapolation: PhD thesis, Stanford University.

Sava, P. and B. Biondi, 2003, Migration velocity analysis by recursive wavefield extrapolation: In: proceedings of the 2003 EAGE-SEG Summer Research Workshop, T21.

———, 2004, Wave-equation migration velocity analysis. II. Subsalt imaging examples: Geophysical Prospecting, **52**, 607–623.

Sava, P. and S. Fomel, 2005, Coordinate-independent angle-gathers for wave equation migration: SEG Technical Program Expanded Abstracts, **24**, 2052–2055.

———, 2006, Time-shift imaging condition in seismic migration: Geophysics, **71**, S209–S217.

Shen, P. and W. W. Symes, 2008, Automatic velocity analysis via shot profile migration: Geophysics, **73**, VE49–VE59.